CALPHAD: Computer Coupling of Phase Diagrams and Thermochemistry 51 (2015) 133–143

Contents lists available at ScienceDirect

CALPHAD: Computer Coupling of Phase Diagrams and Thermochemistry

journal homepage: www.elsevier.com/locate/calphad

Equation of state of solid, liquid and gaseous tantalum from first principles

Ljubomir Miljacic [a,b], Steven Demers [b], Qi-Jun Hong [a,c,*], Axel van de Walle [a]

[a] School of Engineering, Brown University, Providence, RI 02912, USA
[b] Department of Applied Physics and Materials Science, California Institute of Technology, Pasadena, CA 91125, USA
[c] Division of Chemistry and Chemical Engineering, California Institute of Technology, Pasadena, CA 91125, USA

ARTICLE INFO

Article history:
Received 4 May 2015
Received in revised form
23 August 2015
Accepted 25 August 2015
Available online 18 September 2015

Keywords:
Tantalum
Equation of state
Density functional theory

ABSTRACT

We present ab initio calculations of the phase diagram and the equation of state of Ta in a wide range of volumes and temperatures, with volumes from 9 to 180 Å^3/atom, temperature as high as 20 000 K, and pressure up to 7 Mbars. The calculations are based on first principles, in combination with techniques of molecular dynamics, thermodynamic integration, and statistical modeling. Multiple phases are studied, including the solid, fluid, and gas single phases, as well as two-phase coexistences. We calculate the critical point by direct molecular dynamics sampling, and extend the equation of state to very low density through virial series fitting. The accuracy of the equation of state is assessed by comparing both the predicted melting curve and the critical point with previous experimental and theoretical investigations.

1. Introduction

The accurate determination of high-pressure and high-temperature equations of state (EOS) [1] and phase diagrams has fundamental importance in a wide variety of fields. For instance, geophysics and planetary sciences often require knowledge about the response of materials under extreme conditions [2]. There is also an increasing interest in modeling high-velocity impacts [3,4] via multiscale methods, which also demands EOS as fundamental input in a very wide range of conditions.

This paper presents comprehensive calculations of the EOS and the phase diagram of Ta. Our approach is built upon previous investigations [2,5,6] along four main dimensions. (i) It is based on direct ab initio calculations, without relying on any force-field fitting as a stepping stone. This enables us to assess the quality of these force fields concerned. (ii) It covers all phases, including the solid, liquid, and gas phases, and all associated two-phase equilibria. (iii) It includes the effect of electronic excitations. (iv) It delivers not only the phase diagram, but also the free energies of all phases, which serve as fundamental input in multi-scale or finite-element models. We obtain the free energy as a 2D function in a large section of the volume and temperature (V,T) space, with the associated pressure range of 0–7 Mbar, and the temperature range of 0–20 000 K, while the corresponding phases span from high-pressure dense liquids to gas states well beyond the critical point.

Transition metals are known to pose special challenges for density functional theory (DFT) [7–9], in terms of both computational accuracy and efficiency. However, for some transition metals (in particular Ta), the straightforward application of generalized gradient approximation (GGA) [10–12] was shown capable of delivering accurate solid properties and melting curve [2,13], despite the ongoing debates over issues such as the mismatch between diamond-anvil-cell (DAC) measurements and shock experiments data, as well as the possibility of polymorphism in high-pressure solids [14–16]. These previous studies suggest that it is within the reach of modern theory to accurately compute the thermodynamic properties of Ta at the atomistic scale, for a vast range of thermodynamic conditions up to very high pressures, temperatures, and volumes. Carefully constructed numerical procedures and techniques are capable of capturing the information implicitly present in the DFT Hamiltonian to compute thermodynamic functions of states.

To investigate the material behavior across various phases, we rely on a unifying approach of thermodynamic integration. Its most expensive part is the ab initio molecular dynamics (MD) sampling of local material properties at each point with fixed density and temperature, which needs to be independently collected on a 2D grid in the vast (V,T) region. To reduce the computational burden, we employ analytic statistical mechanics modeling where appropriate. This technique also provides a reference point for the integration and allows us to extrapolate

* Corresponding author at: School of Engineering, Brown University, Providence, RI 02912, USA.
E-mail address: qhong@alumni.caltech.edu (Q.-J. Hong).

http://dx.doi.org/10.1016/j.calphad.2015.08.005

beyond the directly calculated region.

Although DFT is now routinely used to calculate phase transitions in dense regions of the phase diagram [17], it is generally considered that it becomes less reliable for the gas phase, where atoms are separated by larger distances on average. The critical point (CP) of the liquid–gas phase transition is an important and universal feature of the EOS, positioned between typical dense solid/liquid region and the ideal gas limit, where first-principles data would be very useful [18]. However, as the CP arguably lies at the frontier of the traditional valid domain of DFT, it is necessary to perform a detailed investigation on a relevant system and to compare the results with experiments. One such system of interest is transition metals like Ta. Experimentally, the determination of critical point parameters (including critical pressure P_c, critical temperature T_c, and critical density here expressed as the critical volume per atom V_c) is a long standing open question for most metals [19], because P_c and T_c are too high to precisely study from experiments [18]. Although there have been a number of experimental and semi-empirical estimates [19–26], their discrepancies are considerable, and thus a fully ab initio approach is helpful to further clarify these results. Finally, if DFT alone can be employed to calculate CP parameters and its vicinity with reasonable effort, this approach can be generalized whenever a material is believed to be accurately represented within the DFT framework.

This paper is organized in the following way. The next section describes the basic technical setup of the work and outlines the thermodynamic integration procedure. Section 3 concentrates on the solid phase, and Section 4 on the fluid. Section 5 elaborates the melting curve calculation, and Section 6 deals with the investigation of the critical point and related issues. Finally in Section 7, discussions and conclusions are presented. 3D interactive figures of the pressure field (including the data set), as well as a movie of liquid Ta in MD, are available as supplementary materials.

2. AB initio methodology

All our calculations are based on ab initio DFT and performed with the VASP package [27]. We employ the projector augmented wave (PAW) technique [28] and a Perdew–Burke–Ernzerhof (PBE) [29] pseudopotential with the 5*p* core electrons relaxed, as such a setup was found satisfactory in previous work [2]. The package implements a finite-temperature formulation of DFT. The variational quantity that is minimized and kept constant throughout a *NVE* trajectory is the sum of the kinetic and potential energies and the electronic free energy of the system. Electronic excitation effects are included as the Fermi-type smearing of single particle energy level occupations, which corresponds to an electronic temperature T_e that is equal to the ionic temperature T_i calculated from the kinetic energy of ionic motion. In order to match T_e and T_i, we thermalized the system at a particular volume until the T_i coincided with the preset T_e within a small tolerance. All subsequent MD runs were performed within the *NVE* ensemble. The time step was chosen to be 2 fs, except at very low densities, where we could gradually increase it up to 6 fs without causing a significant drift in total energy. The lengths of data-gathering trajectories varied in a wide range of 1–20 ps, depending on the temperature, pressure, density, and local density of sampled points in the (*V*,*T*) space. The plane wave energy cutoff was set at 275 eV, providing a total energy error of no more than 7 meV per particle and a pressure error of less than 0.4% at high pressures. We have tested spin polarization effects and reconfirmed their irrelevance. The number of atoms in the simulation cell was 128, except when close to the gas phase, which will be discussed later in detail. The *k*-space sampling was performed using Monkhorst–Pack special points. In the solid phase, all MD runs were performed with a $2\times2\times2$ mesh. In the fluid, total-energy calculations was carried out on the $2\times2\times2$ mesh, while for pressure calculations the Γ-point setup was proven sufficient. In order to evaluate the finite-size effect, we performed tests on a system of 250 atoms at the point of the highest density and temperature, where insufficiencies of our setup were most likely to be noticed. These tests gave no significant change in results and suggested that the finite-size effect was small.

To construct the free energy of Ta in 2D space $F(V, T)$, we employ the method of thermodynamic integration, using the two thermodynamic relations [30]:

$$P = -\left(\frac{\partial F}{\partial V}\right)_T, \tag{1}$$

$$E = \left(\frac{\partial (F/T)}{\partial (1/T)}\right)_V, \tag{2}$$

where P is the pressure, and E the total kinetic and potential energy of the system calculated from MD. As a general procedure, we calculate pressures on a 2D grid of points, and energies on a 1D grid of points at a selected volume, as illustrated in Fig. 1. A fine grid is required so that the fitted analytic functions $P_f(V, T)$ and $E_f(T)$ are smooth and reliable. There exist multiple solutions for the $F_f(T)$ curve constructed by Eq. (2) and $E_f(T)$, because the thermodynamic relation is also satisfied by $F_f(T) - TS_0$ for any arbitrary entropy constant S_0. If this constant is known, the free energy F can then be fully determined anywhere in the (*V*,*T*) region of interest.

As explained later in the text, S_0 was conveniently determined by the knowledge of the melting point T_m, which can be calculated in a variety of ab initio approaches [2,5,6,30–33]. In the case of Ta, this problem was already studied with success. Hence we referred to previous ab initio-based theoretical calculations.

3. Solid phase

The body-centered cubic (BCC) phase of Ta is stable from zero temperature to melting at all volumes. The free energy per particle of Ta can be treated within the quasiharmonic approximation (QA) as

$$F_{QA}(V, T) = F_0 + \frac{E_0(V)}{N} + F_v(V, T) + F_e(V, T), \tag{3}$$

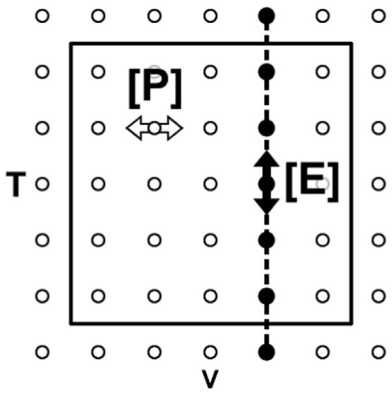

Fig. 1. Thermodynamic integration of the free energy in a finite region of two-dimensional (*V*,*T*) space. The pressure is calculated on a 2D grid of points along the horizontal direction (open arrows), while the total energy changes on an 1D grid of points, for integration in the vertical direction (solid arrows). To avoid extrapolation errors, the grid should fully encompass the selected region, shown as the square.

where N is the number of atoms in the periodic cell and $E_0(V)$ is the reference potential energy per simulation cell at $T=0$, which is provided by the DFT engine and can be offset by a global constant F_0. F_ν and F_e are vibrational and electronic contributions, respectively:

$$F_\nu(V,T) = \frac{k_B T}{N} \sum_m \ln\left[2\sinh\left(\frac{h\nu_m(V)}{2k_B T}\right)\right], \tag{4}$$

$$F_e(V,T) = \frac{1}{N}(E_e(V,T) - TS_e(V,T)), \tag{5}$$

where k_B is the Boltzmann constant, and $\{\nu_m\}$ the set of stable phonon frequencies calculated by finite differences (small atomic displacements), using the "fiftc" command in the ATAT package [34]. The F_e term includes the electronic thermal excitation energy $\int [f_V^T(\epsilon) - f_V^0(\epsilon)]\epsilon g_V(\epsilon)\, d\epsilon$ and the associated entropy increase $k_B \int [f_V^T(\epsilon)\ln f_V^T(\epsilon) + (1-f_V^T(\epsilon))\ln(1-f_V^T(\epsilon))]g_V(\epsilon)\, d\epsilon$, where $f_V^T(\epsilon)$ is the (V,T)-dependent Fermi–Dirac distribution of single-particle states, and $g_V(\epsilon)$ the volume-dependent electronic density of states.

In Eqs. (4) and (5), phonons and energy spectra are calculated with electronic temperature set to zero. The remaining errors of QA, apart from the general flaw of the DFT pseudopotentials, are (i) the temperature dependence of phonons, as excited electrons are pushed into anti-bonding states, and (ii) the anharmonic effects, which become significant near the melting curve. We have tested these combined effects by calculating the free energy from thermodynamic integration F_{TI} (Eq. (2)), in which we run direct MD for two volumes, 10.0 Å^3/atom (where the pressure is in the Mbar scale) and 19.5 Å^3/atom (close to the atmospheric pressure). To fix the open S_0 problem, we have matched F_{QA} and F_{TI} calculated independently from Eqs. (2) and (3) at two temperatures 11 000 K and 1800 K, respectively. We found that as temperatures approach the melting point, omitting the electronic contribution of Eq. (5) leads to total errors of 480 meV/atom and 130 meV/atom, respectively. Including this contribution improves the results and reduces the relative error that is largely volume-independent. Around 3000 K it is reduced by about two thirds, while at 9000 K it is mostly eliminated. This fact suggests that QA is surprisingly accurate for practically all volumes and temperatures in the case of Ta. To remove the remaining small errors of anharmonicity and the temperature dependence of phonons across the whole (V,T) space, we added corrections calculated at these two extreme volumes $\Delta F = F_{TI} - F_{QA}$, and linearly interpolated ΔF for the volumes in-between.

Despite the high general accuracy of QA at the melting temperature, one universal issue remains to be addressed. To cover the solid region in (V,T), we need to perform zero-temperature based QA calculations for large volumes where the BCC lattice thermally expands near T_m. But at $T=0$ such volumes are well beyond the sublimation point and the BCC solid is not stable. Therefore, the QA result may be problematic here as some of the $\{\nu_m\}$ may become physically unstable. In addition, since we chose the melting point at atmospheric pressure as the reference point, we need the precise volume of this point. Therefore, we must independently ensure that the thermal expansion is in agreement with the direct MD result, up to the melting temperature. Note that stabilizing a single phase solid at T_m presents no practical problem in MD, thanks to the limited length of the simulation time.

As Figs. 2 and 3 indeed show, expanding the volume beyond $P=0$ soon leads to increasing uncertainty in F_{QA}. Although the error accumulates to only 30 meV/atom near T_m, it still artificially shifts the zero-pressure volume by ~0.5 Å^3/atom, compared to MD. We exclude the possibility of lattice defects being the cause of this discrepancy. Both QA and MD are based on defect-free structures, hence lattice defects are unrelated to this problem. In addition, the defect density is too low to explain the discrepancy, given the high vacancy formation energy (the values, 2.95 and 6.96 eV at ambient pressure and 300 GPa, respectively [35], amount to a concentration of 3×10^{-5} and 1×10^{-4}).

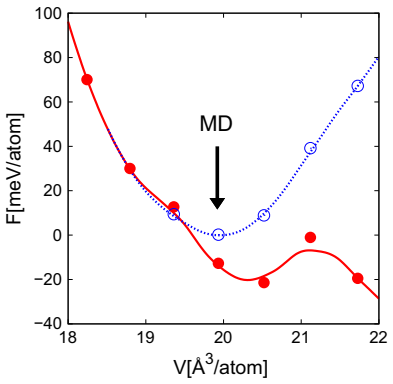

Fig. 2. Correcting the QA free energy at large volumes at 3000 K (near T_m). When the solid volume increases beyond 19 Å^3/atom, F_{QA} (full dots) develops small fluctuations at high temperatures. We add a small entropy term at each volume in this range so that the corrected free energy (open dots) recovers the thermal expansion calculated by MD (arrow). The accurate shape of the corrected free energy at this temperature can be determined from the MD pressures in the vicinity of $P=0$. The curves are interpolations between discrete volumes (dots). The free energy axis is arbitrarily shifted.

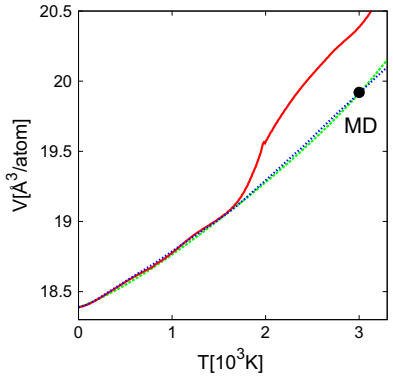

Fig. 3. Correcting the lattice thermal expansion calculated by QA (full line). The mismatch between QA and MD is corrected at the atmospheric pressure and 3000 K (dot), as described in the text. The corrected thermal expansion (dotted line) recovers the MD result (dashed line) for all temperatures.

The fluctuations in Figs. 2 and 3 disappear at low temperatures for all relevant volumes, which suggests that this QA error is entropic. A natural way to address this issue is to add a small entropy-like term $-TS^*(V)$ to the free energy of Eq. (3) for the high volumes, so that the equilibrium volume coincides with MD results at temperatures near T_m. Since the volume is correct at low temperatures and the thermal expansion is smooth and monotonous, such a procedure can be expected to suffice. Fig. 2 illustrates the change in free energy after the correction. The lattice thermal expansion agrees with MD for all the temperatures below T_m, as shown in Fig. 3. Our calculated thermal expansion is $\Delta a_0/a_0 = 6.4324\times10^{-6}T + 8.7229\times10^{-10}T^2$, which compares well with experiments [36,37].

Finally, choosing this form of correction guarantees that the difference between F_{QA} and F_{TI} remains unaffected, as the integration procedure of Eq. (2) also involves adding a constant entropic term $-TS_0$ at a volume of interest. Therefore, if a S^* term is added to the QA free energy, then a $S_0 + S^*$ term in solving Eq. (2)

would keep the $F_{TI} - F_{QA}$ difference unchanged. The two correction procedures are fully independent of each other, and thus can be employed separately.

Currently there is uncertainty in the literature regarding whether the hexagonal ω phase is thermodynamically more stable than the BCC phase in the high-pressure region. One work [15] employs the so-called Z method [38] (though the validity of the Z method has been questioned [16,39,40]) and performs DFT-based MD simulations on various cell sizes from 32 to 144 atoms. It predicts that the hexagonal ω phase melts at higher temperatures than BCC does. In contrast, MD simulations on very large supercells suggest that this finding is an artifact of finite size effects. Using the same method with a MGPT force field [16], these simulations show that the BCC phase is always more stable in large supercells.

We have studied this issue with our own approach. The Z-method work [15] relies on a special pseudopotential with 4*p* inner core electrons included (not available in the standard VASP package) that is different from the pseudopotential used in the present work. Hence, the effects of the 4*p* and 5*p* inner-core electrons are first evaluated. We have compared their result (at T=0) against other pseudopotentials, as shown in Fig. 4. We start from the pseudopotential with the fewest valence electrons and gradually relax the inner core electrons. The ratio c/a is sensitive to the quality of the pseudopotential, as adding the 5*p* electrons significantly improves the results. However, further inclusion of the 4*p* electrons leads to negligible effect even at high pressures. This suggests that the standard pseudopotentials are accurate enough for our task.

We have performed direct MD simulations of the hexagonal ω phase for various volumes and temperatures near the melting point of BCC phase. The simulations are performed with 135 atoms in the supercell, with *k*-space sampling on a $3\times3\times3$ mesh. All samples show that the hexagonal ω phase transits to a distorted BCC phase rapidly. When c/a ratio was subsequently changed to the "ideal" BCC value of 0.6124, all samples relaxed to pressures and energies identical to the BCC phase. Alternatively, we performed a set of MD simulations on two-phase coexistence [33] of the hexagonal ω and liquid phases. The simulations are carried out with a small supercell of 162 atoms under the *NPT* ensemble. The same rapid transition to the BCC phase was observed in these simulations. Thus, our result corroborates the findings of [16], but on the basis of a fully ab initio method.

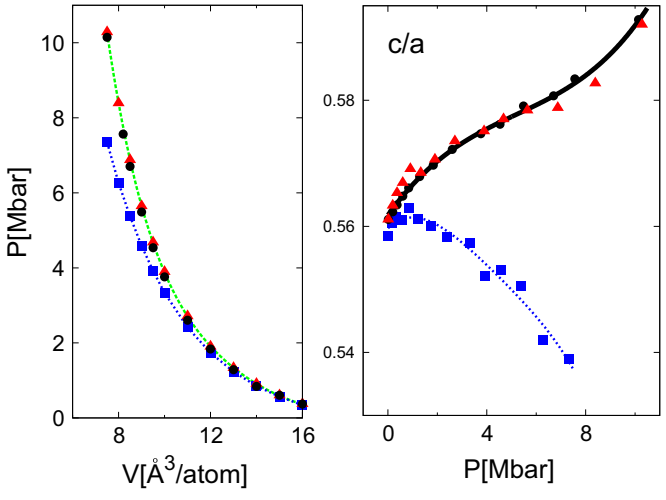

Fig. 4. Comparison of various pseudopotentials: 6*s*5*d* (squares), 5*p*6*s*5*d* (triangles), and 4*p*5*p*6*s*5*d* (circles) electrons. The 4*p*5*p*6*s*5*d* data is from [15] while the others are from the present work. The 5*p*6*s*5*d* pseudopotential was used in this work to obtain the equation of state. All calculations are carried out at $T=0$. Dashed and dotted lines serve as eyeguides. Left: *P*–*V* relation in the BCC phase; right: c/a ratio and pressure for the hexagonal-ω phase.

4. Fluid phase

The free energy of the fluid phase is determined by straightforward thermodynamic integration as illustrated in Fig. 1. The constructed representation of the pressure field $P(V, T)$ is shown in Fig. 5, which is divided into two parts at $V=40$ Å^3/atom for better visual presentation. The discrete sets of points in the figure are directly based on data sampling. In order to achieve a smooth, analytic and locally accurate representation of the pressure field that spans over three orders of magnitude, we employ a fitting procedure as follows. We utilize a general 2D polynomial in the form $\sum_{i,j}^{n,m} c_{i,j} V^i T^j$, where both the polynomial orders and coefficients are determined through fitting. First we perform a global data fit to obtain the (n,m) pair which minimizes the cross-validation score [41]. Then, using the selected polynomial orders of (6, 5), we uniformly divide the volume axis into 30 overlapping segments and perform a fit in each segment separately. To stabilize these fits, we add a number of points between the sampled data, as their scattering is small enough to make such interpolations reliable. Finally, we smoothly connect the overlapping fits into the whole pressure field $P(V, T)$, which accurately represents all the actual pressure data that we collected.

To reach the high-volume region in Fig. 5, the size of the simulation cell had to be reduced to 64 atoms above 40 Å^3/atom and 32 atoms above 80 Å^3/atom, otherwise the simulations would become unfeasibly slow. Our tests suggest that the error

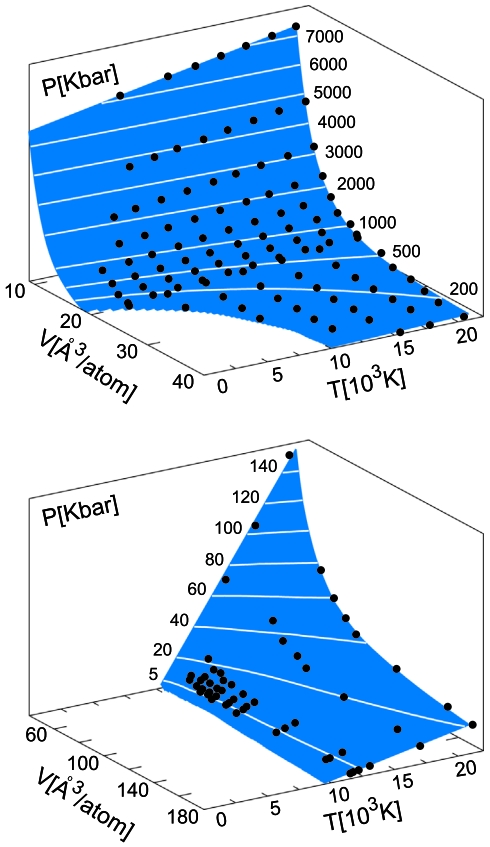

Fig. 5. Fluid pressure field (surfaces) with sampled pressure data points (dots), as described in the text. Isobaric lines are added to guide the eye. Only positive pressures are shown. Notice the changes of scale on the volume and pressure axes between the two figures. 3D interactive figures are available in the supplementary materials.

introduced in this fashion is of the order of statistical errors and thus negligible.

While the free energy inside the single-component fluid phase can be determined via thermodynamic integration from the ideal gas limit, the solid phase cannot be reached in this fashion, because thermodynamic integration fails upon phase transition. As a result, there remains a free parameter, which measures the free energy difference between the solid and the liquid. In principle, this parameter could be determined using the quasiharmonic approximation and the ideal gas model as reference states for the solid and liquid phases, respectively. However, such an approach may be very sensitive to numerical and statistical noise due to the long integration paths. To avoid this problem, we instead use the melting point at the atmospheric pressure T_m. We directly match the free energies of the two phases at the melting point to determine the aforementioned free parameter. In this way the integration paths are kept short.

The task to calculate T_m has been previously accomplished for Ta, and we take results of two particular publications [2,42] that employ an identical level of ab initio theory. The employed methodology is a perturbative DFT correction to melting temperature calculations previously performed on a classical force-field (FF), which we will discuss later. Their calculated melting points of 3326 and 3170 K do not perfectly match because they use different FF's, but ideally such techniques could be repeated independently until an average value is obtained. For our purpose we take the medium T_m=3248 K as the established theoretical result. This value also compares well with our recent direct DFT calculation of the melting temperature (T_m = 3195 ± 41 K) [33]. On the experimental side, T_m varies in the range of 3213–3290 K [43,44]. Therefore, the agreement between the cumulative experimental and theoretical efforts is satisfactory.

The integration procedure is executed as follows. First, by observing the solid free energy and the fluid pressure field in the vicinity of T_m, we can determine the two volumes where $P=-(\partial F/\partial V)_T=0$, which encompass the solid–liquid coexistence region. We select a volume V^* inside the coexistence region between these two ends, in this case 21.0 Å^3/atom. Then, we integrate Eq. (2) along a temperature line at V^*, by performing several MD runs in both the solid and liquid phases. We fit the two $E(T)$ models by accurate polynomials. The 1D integration procedure is completed by the constraint that fluid free energy at (V^*, T_m) coincides with a numerical value which, after integration towards higher volumes, produces a common-tangent line of $P=0$ with the solid free energy at T_m. The complete 2D single-phase fluid free energy is then determined straightforwardly as an extension away from V^* line at all temperatures, via pressure field analytical integration.

5. Melting curve

With the solid and liquid data prepared with sufficient accuracy, extraction of the melting curve is a straightforward numerical procedure of locating the array of common tangents between the solid and liquid free energy curves across a temperature range. However, the solid and liquid free energies are typically very close, so the locations of melting points are often sensitive to the underlying data. At each temperature, we employ local quadratic fitting of the free energies, and then solve the common tangent analytically as we connect the two parabolas. Fig. 6 shows the V–T relation for the solid and liquid phases as the two lines encompass the solid–liquid coexistence region $[V_S(T), V_L(T)]$. Since the fluid free energy is built and fitted upon a collection of dispersed pressure points, both V_S and V_L show some excessive oscillations, which can be subsequently removed in several ways. Improving

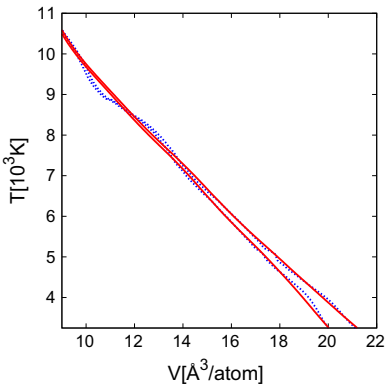

Fig. 6. Melting curve in V–T plane. V_S, V_L lines encompass the solid–liquid coexistence region, before (dotted lines) and after (full lines) the a posteriori smoothing procedure.

the general sampling statistics of the dataset is too costly since too many points must be improved redundantly. Reducing the overall flexibility in the fitting of the liquid pressure may unnecessarily reduce its overall accuracy. We thus resort to a posteriori smoothing of $V_{S,L}$ by averaging them at each point over a surrounding interval. The minimal width of the interval is chosen such that local fluctuation disappears and only the general trend of $V_{S,L}$ remains. The melting curve is then fully resolved as a string of points on the liquid pressure field at $P(V_L(T), T)$.

In the literature there are several publications that calculate the melting curve of Ta, all done via classical atomistic simulations with ab initio corrections. As shown in Fig. 7, these results include (a) qEAM, an extended 19-parameter FF of embedded atom model (EAM) type, which is fitted mainly to zero-temperature DFT data, with the melting curve calculated from a coexistence method [5], (b) MGPT, an extended volume-dependent FF with up to 4-body terms, which is fitted to various theoretical and experimental sources, with melting points calculated from direct melting within periodic cell, corrected for hysteresis effects [6], and (c) a reference EAM FF optimized at low and medium pressures for the liquid, with free energy corrected to DFT Hamiltonian perturbatively, and with melting curve calculated from coexistence simulations [2]. The DFT input in all these approaches is on the same GGA level of theory as this work.

At zero pressure, all these theoretical predictions fall close to the experimental range, except for a slight overestimate by MGPT. The melting curve from MGPT largely coincides with qEAM and our result at pressures up to 1.5 Mbar. In the high pressure region, only one shock-wave compression measurement at 3 Mbar [45] is available with a wide error margin of 1500 K. The MGPT approach is the only one that fails to agree with it. Our curve essentially overlaps with the qEAM data, naturally continuing them into higher pressures. Result (c) stands apart from others in the low pressure region, while still agreeing with the high-pressure experimental measurement within the error bar.

The dT/dP slope at zero pressure is another quantity to benchmark. The experimental value is 6 ± 1 K/kbar [46], while previous theoretical estimate of the qEAM method [5] gives 9.3 K/kbar. Extracting such information from our curve requires an additional step of smoothing. We performed 2nd and 3rd order polynomial fits to the data shown on the right panel of Fig. 7, up to 0.6 Mbar. This gives estimates of 6.6 and 7.7 K/kbar, which are in good agreement with experiments.

Our experience in melting temperature calculations [33,42,47–51] enables us to readily capture theoretical melting temperatures from different first principles approaches. Here we employ our recently developed small-size coexistence method, which is

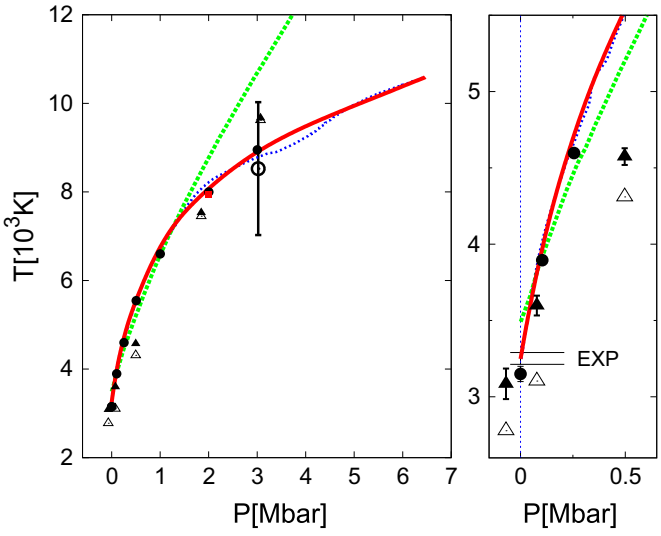

Fig. 7. Melting curve calculated from various approaches: (a) qEAM [5] (dots), (b) MGPT [6] (dashed line), (c) EAM result (open triangles) with DFT correction [2] (full triangles), and this work (full line). Also shown are our results before the smoothing procedure (dotted line) and the melting point calculated by the small-size coexistence method (full square in red, at 2 Mbar and 7953 K). At the high-pressure end, most theoretical predictions fall within the error bar of the shock measurement (open circle). The right panel shows the low-pressure region in more detail. Experimental T_m measurements are within the range of the two horizontal lines. (For interpretation of the references to color in this figure caption, the reader is referred to the web version of this paper.)

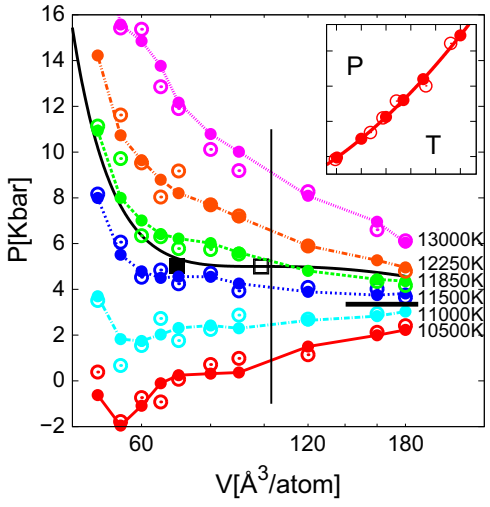

Fig. 8. Data used for elucidation of the ab initio CP (full square). Direct MD averages (open circles) are fitted by quadratic functions at every volume (full circles) to represent the pressure field around CP, as shown in the inset. Simulations are performed with 64 atoms on the left of the thin vertical line and with 32 atoms on the right. The full black line shows the critical isotherm of a Peng–Robinson model with $\{P_c,T_c\}$ set to match the estimated ab initio values, with its CP shifted to a higher volume (hollow square). The short thick line is an estimate of the binodal line (see text). The volume axis is logarithmic.

capable of determining the melting temperature directly from first-principles at a relatively low cost. The details of our method have been described in Ref. [33], where its validity and flexibility are extensively demonstrated. For consistency, we employ the same pseudopotential and DFT setups as we used to generate the EOS and melting curve. At 2 Mbars, we generate duplicated configurations of BCC-solid and liquid coexistences (162 Ta atoms) and run first-principles *NPT* MD to simulate their evolutions, through which we determine the melting temperature based on a statistical analysis of the thermodynamic fluctuation of the solid–liquid interface. This approach predicts the melting temperature as 7953 ± 69 K, as shown in Fig. 7. This melting temperature is in good accordance with our melting curve calculations.

6. Critical point

Direct calculations of the critical point (CP) of the liquid–gas phase transition in materials are traditionally done in the context of atomistic empirical potential fitting, as they were previously considered too costly for a purely ab initio approach [52]. This is even more pronounced for strong binding systems like Ta, where the gas side of an isotherm soon reaches extremely large simulation volumes, as the temperature falls below T_c. Thanks to the increasing computer power, we demonstrate the feasibility of such a task through a carefully structured series of MD runs.

We first roughly located the CP through a sparse search of the pressure field across the low density regions of the (V,T) space. Then we calculated several surrounding isotherms in detail. For each volume, starting from the $T^*=13\,000$ K isotherm, which is slightly above the estimated T_c, we gradually decreased the ionic and electronic temperature via velocity rescaling. Since the pressures were low, this change in kinetic energy would not significantly affect the potential energy, and thus only a minor rearrangement of the atomic structure was observed. After a short thermalization for a few picoseconds, we collected the data for an additional period of 10–20 ps. In this way the system is likely to remain as an undercooled fluid and avoid the onset of phase separation during the short time scale of simulation. (Such an onset was nevertheless observed in a few cases as a sharp change in temperature and pressure. For these cases we would increase the temperature to T^*, which provides us a different starting geometry for the subsequent quenching.) The results are collected in Fig. 8. The vertical line divides the data according to the system size, with 64 atoms on the left and 32 atoms on the right. To minimize the associated error, we have pushed this line to the right as much as possible until simulations became unfeasibly slow. Similarly, we used 128 atoms for volumes below 40 Å^3/atom, as same as our model in the previous sections. We find that this bias of system-size change was small compared to the statistical fluctuations in the data, thus allowing us to seamlessly move across the data calculated at various system sizes.

We calculated six isotherms with temperatures in the range of 10 500–13 000 K, shown in Fig. 8. Since the averaged temperature will slightly deviate from the desired target value of the *NVE* ensemble, we fit the pressure data separately at each volume with a quadratic polynomial, and use it as the final two-dimensional $P(V, T)$ representation. The inset figure illustrates the reduction of the overall statistical error.

We use the calculated pressure field to plot isotherms with small temperature increments to locate the CP, as illustrated in Fig. 9. We approximate the errors associated with the remaining statistical fluctuations of the pressure data by the following "bootstrap" procedure [53]. Assuming that the fluctuations are not affected by the density and temperature in the vicinity of CP, we calculate the average standard deviation of the calculated pressures from their respective quadratic fits, which gives $\sigma^* = 0.058$ kbar. We then replace each calculated point by a normal distribution around each fitted line with a width of σ^*, and we repeat the quadratic fitting procedure. A new location of the CP is estimated by finding the isotherm with the highest temperature such that the condition $dP/dV > 0$ is satisfied in a certain segment. The middle point of such a segment is then taken as a new (P_c,T_c,V_c) sample. We repeat this procedure for 10^4 times, and the region of pressure and temperature that contains 2/3 of the sampled CP's is considered as the error bars. Finding the error in

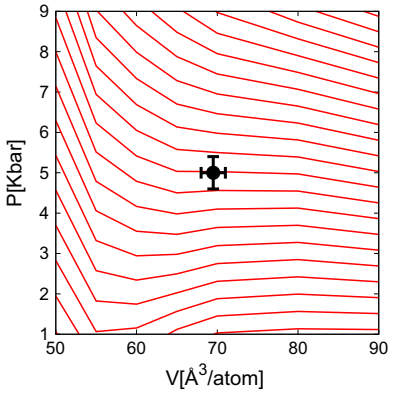

Fig. 9. An array of quadratic pressure fits that enables us to determine the precise position of the CP (dot), based on the study of arbitrarily close isotherms (lines) and error analysis. The error bars reflect the magnitude of the statistical uncertainty in the predicted CP.

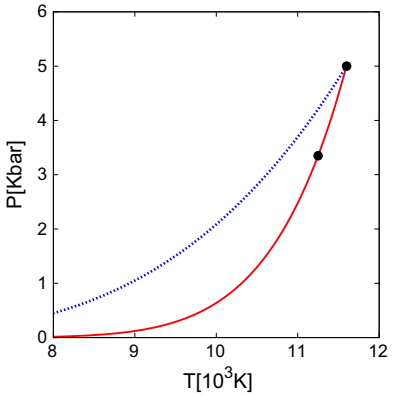

Fig. 10. Vapor pressure (full line) based on a fit using the two ab initio data points (circles) on a binodal line. The upper point is the CP and lower one an estimate of the binodal line. Also plotted is the vapor pressure of the Peng–Robinson model (dotted line) with the same $\{P_c, T_c\}$.

volume is less straightforward because the volumes sampled in our calculations are discrete and highly repetitive. Here, we find the unique normal distribution that produces the same discrete distribution of V_c samples. The mean and the width of such a distribution are the final V_c and the associated error. Thus, the fully ab initio CP parameters are estimated as $T_c = 11\,600 \pm 90$ K, $P_c = 5.0 \pm 0.4$ kbar, $V_c = 69.5 \pm 1.5$ Å^3/atom. These error bars are shown in Figs. 9 and 11.

It is interesting to compare the calculated pressure field in the vicinity of the CP with simple two-parameter models of the van der Waals type. We choose a well performing Peng–Robinson (PR) model [54], which is specified by two critical parameters $\{P_c,T_c\}$. The full line in Fig. 8 is the critical isotherm of the PR model when $\{P_c,T_c\}$ are set to the values of the ab initio estimates. V_c here is shifted to 98.7 Å^3/atom, and accordingly the pressure declines more slowly with volume. To estimate the vapor pressure in the liquid–gas coexistence region, we fit the pressure with a standard ansatz [55] $\log P_{\mathrm{vap}} = a - b/T$, which needs two data points to elucidate the a and b parameters. The CP serves as one data point. For the other point we use the fact that the binodal line becomes flat and it approaches the vapor pressure at large volumes for a temperature just below the critical point. We find that the pressure decreases with volume in the large-volume region on the 11 500 K isotherm curve (which suggests a gas phase), while it increases for the 11 000 K isotherm curve. Hence we can assume that the binodal is trapped between these two lines for large volumes, which gives an estimate of $P_{\mathrm{vap}}(11\,250\ \mathrm{K}) = 3.35$ kbar. We fit the parameters to $a = 14.482$ and $b = 149\,320$ K. Fig. 10 shows the difference between our results and the PR model, whose P_{vap} curve also follows this simple ansatz $\log P_{\mathrm{vap}} = a' - b'/T$ closely. We also calculated the binodal line to the left of the CP in the P–V diagram, by finding a horizontal line where the liquid pressure equals P_{vap} on an isotherm. The result again suggests that the ab initio binodal differs notably from the PR one.

Accurate determination of the CP of all but the simplest metals is an ongoing problem for the experimental community. For Ta, widely scattered estimates were given over the years, as shown in Fig. 11. However, while most of these estimates are from indirect semi-empirical theoretical approaches that are based on correlation of various metallic properties with critical parameters (such as ionization potential, heat of vaporization, and cohesive energy, etc.), one experimental group recently performed the most direct measurement so far by quickly heating the metal and approaching CP via the spinodal line [19]. Their work is expected to be of higher quality than previous attempts. In this view, it is satisfactory that our ab initio estimate of the CP parameters is the closest to this particular measurement.

The PR model, although unable to accurately represent the pressure in the vicinity of CP due to the V_c mismatch, proves useful in the study of the quality of various $\{P_c,T_c\}$ estimates. To this effect, we calculate the pressure difference between the ab initio and PR models as the standard deviation $\delta P_{\mathrm{PR-DFT}} \sim \langle (P_{PR} - P_{DFT})^2 \rangle^{1/2}$ on a finite set of data points above the critical isotherm (full circles in Fig. 8). This quantity measures the quality of PR models with various parameters. The deviation is minimized when the PR parameters $\{P_c,T_c\}$ coincide with ab initio, so it can quantify the disagreement between these two CP estimates in a metric proportional to the corresponding disagreement in physical observables. (Two apparently distant CP may be associated with very similar pressures fields $P(V, T)$.)

In the aforementioned procedure to determine the error bars of the CP parameters from statistically sampling, (P_c,T_c) pairs are highly correlated in the P–T diagram, with points falling on a straight line L, as shown in Fig. 11. The direction of L closely agrees with the direction that minimizes $\delta P_{\mathrm{PR-DFT}}$ as the PR parameters vary. We thus interpret the line L as a set of $\{P_c, T_c\}$ pairs such that their underlying pressure fields resemble the DFT results. Moving

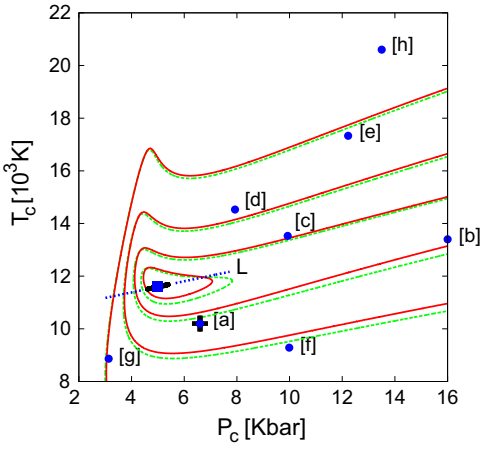

Fig. 11. Previous studies (dots) of the CP parameters, together with our ab initio estimate (square): [a] [19] (with error bars), [b] [20], [c] [21], [d] [22], [e] [23], [f] [24], [g] [25], and [h] [26]. We keep the square bracketed designation of these results throughout this paper. The straight line L (dotted), which passes through our estimated CP, is the statistically sampled (P_c,T_c) pairs, as described in the text. 2/3 of these pairs fall within the thick segment of L (full line), representing error bars of the final P_c and T_c estimates. Isolines of constant $\delta P_{\mathrm{PR-DFT}}$ (full line) and $\delta P_{\mathrm{PR-PR_0}}$ (dashed line) indicate the similarity of the pressure fields compared to the ab initio result.

away from L yields a readily detectable change in the shape of the pressure field.

Finally, we change the benchmark to the PR model (PR_0) with ab initio parameters, which minimizes δP_{PR-DFT}. We calculate δP_{PR-PR_0} on the same set of points, for different PR models with $\{P_c,T_c\}$ parameters. As Fig. 11 shows, this function does not significantly differ from δP_{PR-DFT}. In the vicinity of CP, fitting the PR model to a small number of pressure data points gives the same $\{P_c, T_c\}$ estimate as an elaborate statistical analysis does, as well as the same direction of minimal error L and the error function δP_{PR}. Therefore we find that the ab initio pressure field can be fully substituted with the PR_0 one, for the analysis of the P_c-T_c diagram.

We can then assign this simple model field to previous CP estimates. Though we do not actually have these pressure fields but only their respective $\{P_c, T_c\}$ estimates, each estimate assumes an underlying pressure field, and we assess its quality via the deviation from ab initio or experimental pressures. Since we are here mainly concerned with the DFT results, this alternative metric is limited only by the general accuracy of the DFT engine used, which is the precise positioning of estimated $\{P_c, T_c\}$. Still, we can partition P_c–T_c diagram by isolines of sharply rising δP_{PR-DFT} (2, 4, 8, and 16 kbar) as a visual help in roughly dividing the previous estimates into three groups, [a–c], [d–f] and [h], with descending agreement with the first principles result, as shown in Fig. 11. In this metric, although result [b] is far in absolute $\{P_c,T_c\}$ values, it still assumes a very similar pressure field to DFT one, while the opposite holds for estimate [f]. The measurement [a] is closest in both criteria.

In order to move from the semi-discrete pressure field representation in the P–V diagram to a fully continuous one, we employ the truncated virial expansion series [56,57]:

$$\frac{PV}{Nk_BT} = 1 + \sum_{i=1}^{n} a_i(T)\left(\frac{N}{V}\right)^i, \tag{6}$$

where N/V is the number density of the system, and k_B Boltzmann's constant. Since our data is fully ab initio, there is no straightforward way to break the system's Hamiltonian into a sum of many-body interactions, and Eq. (6) necessarily involves a polynomial fitting, with temperature-dependent coefficients a_i.

For the fit we use the data points at and above the critical isotherm at 11 600 K, as shown in Fig. 12. In order to closely follow the pressure at and just above CP, the fitting order n has to be raised to 6, reflecting the relevance of many-body interaction in this region. However, signs of overfitting inevitably start to show because the curvature of the critical isotherm is of comparable scale of the statistical fluctuations. Thus such a fit cannot be reliably used to extrapolate the virial EOS toward infinite volume per atom, as further tests confirmed. When the fitting order is reduced to 4, extrapolation is very smooth and it agrees with the ideal gas limit perfectly. The question of the best choice for n thus remains problem dependent. All the fitting coefficients a_i are smooth and monotonous functions of T. But due to the very high T_c of Ta, they converge to their final values at much higher temperatures than explored here.

7. Discussion

7.1. Free energy F(V,T)

The free energy $F(V, T)$ in a vast range of volume and temperature with $V \in [9, 180]$ Å^3 and $T \in [0, 20\,000]$ K can be found as the online supplemental dataset. These data are useful as they provide important thermodynamic properties. For instance, from the free energy we compute the enthalpy under ambient pressure, according to the thermodynamic relation

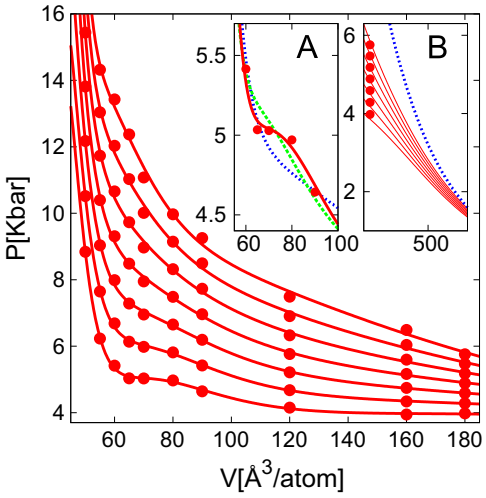

Fig. 12. Virial expansion representation of the pressure field. The pressure data (dots) is fitted (lines), starting from T_c in increments of 200 K. Inset A: datapoints at the critical isotherm (dots) are fitted with polynomial order 6 (full line), 5 (dashed line), and 4 (dotted line). Inset B: order 4 fits (full lines) can be reliably extrapolated toward much larger volumes. The highest T isotherm is shown meeting with its ideal gas counterpart (dotted line).

$$H = \left(\frac{\partial(G/T)}{\partial(1/T)}\right)_p.$$

As shown in Fig. 13, the calculated values are in good agreement with experiments [58]. The heat capacity of the liquid, which is the derivative of enthalpy, is 42.9 and 45.8 J K^{-1} mol^{-1} at 3720 and 5490 K, which closely agree with the experimental value of 41.84 J K^{-1} mol^{-1} [58].

7.2. Electronic excitation

In this work, electronic excitation is accounted for as a Fermi–Dirac distribution over the GGA electronic density of states. While this treatment of electronic excitation is widely used and standard [60–62], GGA has flaws in the description of unoccupied bands, and hence the validity of this approach requires further scrutiny.

Our study shows that this approach is capable of providing a high accuracy. We evaluate the effect of electronic excitation as $F(T_e) - F(0\text{ K})$, where F includes electronic free energy. The electronic temperature T_e affects the spread of the electron population on the density of states, according to Fermi–Dirac distribution. Calculations are performed on snapshots of MD trajectories, hence the results, as ensemble averages, reflect true electronic excitation under the corresponding DFT functional. At low temperatures, the effect of electronic excitation is small and negligible. For example, this effect is only 3 meV/atom for aluminum near its melting point

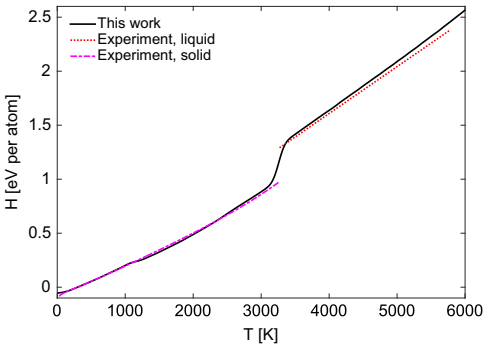

Fig. 13. Enthalpy of tantalum from calculations and experiments.

(~1000 K). While electronic excitation becomes nontrivial at high temperatures, the errors mostly cancel out in the study of phase transitions between two individual phases. This trend is particularly true for metals. Take the melting of tantalum at ambient pressure for example. As shown in Table 1, the electronic excitation free energy for solid-state tantalum is 145 and 114 meV/atom, according to the PBE and Heyd–Scuseria–Ernzerhof (HSE) [59] functionals, respectively. This makes the HSE correction 31 meV/atom, which we may consider as the error of PBE (since the HSE functional generally provides a better description of band structure). While this amount appears large, it is nearly canceled out with its liquid-state counterpart of 33 meV/atom. Thus the overall error from electronic excitation is only 2 meV/atom, when we combine the two phases to determine the melting temperature.

Our treatment of electronic excitation has a clear advantage – it is simple and it costs little, while it still provides a fairly good accuracy. While post-GGA methods may improve on this issue, they are prohibitively expensive when used in conjunction with large-scale molecular dynamics.

7.3. Melting curve

Compared against previous theoretical studies, this work presents a direct translation of DFT Hamiltonian into thermodynamic functions of state in a wide span of space. It can thus serve as an ab initio point of reference. The concurrence of our melting curve with qEAM and MGPT below 1.5 Mbar strongly suggests that all DFT effects are fully captured. Since all these calculations involve basically the same quantum mechanics input, they should give similar outcomes, at least at the lower temperatures where qEAM and MGPT potentials are elaborately fitted. This is indeed true. Our results show remarkable agreement with qEAM in all the reported data points. This is surprising since the FF was fitted mainly to zero-temperature DFT data, with an exception of experimental input of the vacancy formation energy. Ref. [5] reports that qEAM reproduces experimental data up to 3000 K, such as the thermal expansion and melting temperature. We now confirm that the melting curve is practically indistinguishable from the full ab initio results up to very high temperatures. The perturbative EAM+DFT result (c) agrees with other methods in the vicinity of zero pressure, which confirms the validity of the approach in the low-pressure region where the classical EAM part is capable of resembling the real DFT interaction. However, the EAM result underestimates the temperature by more than 1000 K at 0.5 Mbar, and the DFT correction based on perturbation theory fails to recover the full DFT result. Although further study would be required to clear this issue, we can tentatively conclude that the classical potential is not accurate enough for the perturbative treatment. We have thus changed the resulting melting temperature (in Section 4) not as quoted in the publication, but as the linear interpolation of the first two data points at zero pressure, $T_m = 3326$ K. It may be worth noting the advantage of our method. While other approaches require a specific attention on setting up a simulation strategy to elucidate the sensitive melting curve information, in our work the melting curve is a numerical byproduct and its extraction can be largely automated. The melting curve is only a fraction of the large task of constructing a comprehensive and accurate free energy representation, where the main effort is concentrated.

Table 1
Electronic excitation (in eV per atom), comparing PBE and HSE.

Material	T (K)	PBE		HSE		HSE–PBE	
		Solid	Liquid	Solid	Liquid	Solid	Liquid
Al	1000	−0.0035	−0.0038	−0.0030	−0.0032	0.0005	0.0006
Ta	3300	−0.145	−0.148	−0.114	−0.115	0.031	0.033

7.4. ω phase

The existence of stable hexagonal ω phase in Ta is still an open question [15,16]. In our DFT simulations, the hexagonal ω phase is not stable in its dynamic, high pressure and temperature form.

7.5. Multiphase EOS diagram

Combining the fluid pressure field with the vapor pressure, P_{vap}, we can calculate the left binomial of the liquid–gas transition as the locus of points where these pressures are equal, but only the outset of the right binomial since it moves towards extreme simulation volumes very rapidly with decreasing temperature, due to strong attraction between Ta atoms. With our approach we cannot fully trace out this section of the binodal curve that separates two-component liquid–gas and pure gas phases below T_c, since simulation volumes that are required to explore a gas are unattainable by orders of magnitude. This leaves the pure gas phase as the only unresolved part of the V–T diagram.

Putting all these results together, a comprehensive multiphase EOS diagram is established, as shown in Fig. 14. The free energy and the pressure fields extend over a very large section of the (V,T) space, with volumes from 9 Å^3/atom to infinity, temperatures up to 20 000 K, and pressures over 7 Mbars. These fields are accurately represented by piece-wise analytical surfaces.

7.6. Critical point

The ab initio calculation of the critical point of Ta is a useful addition to a group of largely dispersed previous estimates. It includes all relevant electronic contributions. This was achieved via carefully controlled MD runs. After a rough search in the V–T diagram for evidence of negative compressibility $-(\partial V/\partial P)/V$, several surrounding isotherms were calculated within the *NVE* ensemble, while ensuring that the system remains in the single-component metastable fluid state during the data gathering around T_c.

The two metrics we employ to access the quality of previous CP estimates bring out interesting details. First, in both the absolute values of the CP parameters and the similarity of the pressure fields, our data is closest to the only available direct measurement

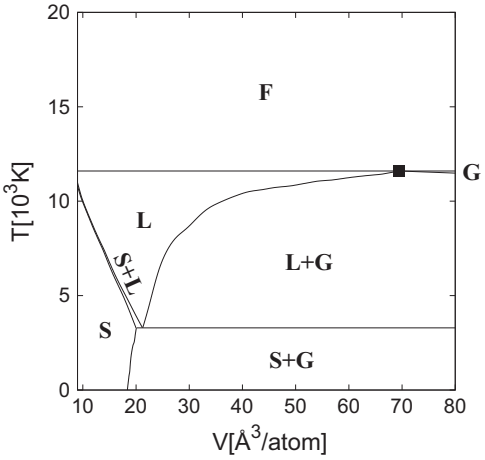

Fig. 14. Complete ab initio diagram of the thermodynamic phases of Ta, including solid (S), liquid (L), gas (G) and fluid (F) phases, and their coexistence regions. The square dot marks the critical point.

[1]. The confluence of these two independent results (one fully based on experiments and the other fully ab initio) strongly suggests that the true location of CP can be greatly narrowed to their vicinity. Estimate [b] is based on cohesive energy argument and an empirical EOS, which was composed from a large collection of experimental data. Although it overestimates P_c by more than a factor 2, Fig. 11 shows that it implies a pressure field very similar to ours, which implies high general accuracy of the empirical EOS. Result [c] also constructs a good quality pressure field but the authors provide few details regarding how this empirical estimate was made. The estimates from the next group ([d–g], in declining quality) are based on similar approaches of employing atomistic models. [d] and [f] employ soft-sphere, [e] a hard-sphere van der Waals, and [g] overlapping virtual atoms models, parametrized by indirect experimental data such as liquid density near CP, cohesive energy, ionization potential, and scaling arguments. Interestingly, reducing sophistication of these models does not introduce a significant decline in predicting CP, with the soft sphere models being better performing. Finally, the semi-empirical estimate [h] based on the heat of vapor data overestimates both P_c and T_c by almost two-fold and implies a very inaccurate pressure field.

As a way to independently assess the validity of the various estimates, we have calculated the $\delta P_{\mathrm{PR-PR_0}}$ isolines by using as reference PR parameters the experimental ones of [a]. The relative ranking of earlier results remains largely unchanged, with line L having the same slope and the only notable difference relative to our ab initio assessment being that the soft-sphere estimate [f] now seems more accurate, while the empirical estimate [c] appears less so.

The performance of PR model points to a number of ways it can be applied outside the ab initio context. For example, when only a set of CP estimates is provided, PR can be used to quickly suggest the outliers. Or, if a CP is considered known for a material, the quality of an EOS model can be tested via δP_{PR} metric by its own CP prediction.

We have shown that the CP can be calculated within reasonable effort directly from first principles as a generic approach. In Ta, the estimated density at the CP is nearly four times lower than in the solid at atmospheric pressure, yet the agreement with the experiment is excellent, implying that the inaccuracy of the DFT approach that occur at larger interatomic separation has no significant effect for CP determination. Furthermore, fitting the ab initio pressure field to virial power series results in an EOS that can be reliably extrapolated to ideal gas at temperatures above the critical point. Below T_c, the available information is shown sufficient to estimate P_{vap} curve.

7.7. The effect of lattice defects

Recent research [63,64] reveals that lattice defects may play an important role in the process of melting. In the case of tantalum, our study suggests that vacancy has little impact on melting temperature. We evaluate the effect of vacancy by computing its concentration in the solid phase. As discussed in Section 3, the high vacancy formation energy suggests a very low defect density (less than 1×10^{-4}), and hence we conclude that its effect is negligible. At temperatures near the melting point, we model the solid phase using molecular dynamics simulations, so in principle we should have caught the spontaneous formation of point defects if they are relatively common. The fact that we do not see such defects is a good indication that our free energies are reliable.

We note that the formation of lattice defects have hitherto been considered as a kinetic process of melting, and it is well known that one does not need to model the kinetic process of the phase transformation in order to locate phase transition boundaries. Instead, free energies analysis is sufficient [48,65–67]. While lattice defects could in principle affect the free energy near the phase transition, their effect should be negligible if they are rare (low in concentration, transient near melting temperature, as the case of tantalum).

8. Conclusions

In conclusion, we have constructed, from first principles, an EOS and a phase diagram of Ta that show good agreement with the available experimental data both in the very high density region (melting curve) and in the highly dilute region (critical point), while its accuracy in the solid was established. This study covers all phases, including the solid, liquid and gas phases, and all associated phase transitions. This EOS is accurate enough to be useful for the analysis and clarification of previously published efforts in calculating sensitive thermodynamic features. Since our approach does not require a FF to be generated, it may be the only available method for the calculations of EOS in wide spans of the phase space for many complex, emerging materials whose energetics is hard to parametrize in such a way. The free energy and pressure surfaces, sampled on a 2D V–T grid of points, are provided as supplemental material.

Acknowledgments

This material is based upon work supported by the Department of Energy National Nuclear Security Administration under Award no. DE-FC52-08NA28613, by the US Office of Naval Research under Grant N00014-12-1-0196 by the National Science Foundation through TeraGrid and XSEDE resources provided by NCSA, SDSC and TACC.

Appendix A. Supplementary data

Supplementary data associated with this article can be found in the online version at http://dx.doi.org/10.1016/j.calphad.2015.08.005.

References

[1] J.R. Macdonald, Rev. Mod. Phys. 41 (1969) 316;
V.N. Zharkov, V.A. Kalinin, Equation of State in Solids at High Pressures and Temperatures, Consultant Bureau, New York, 1971;
M. Sadeghi, G.A. Parsafar, J. Phys. Chem. B 116 (2012) 4943;
T. Qin, R. Drautz, D.G. Pettifor, Phys. Rev. B 77 (2008) 220103(R);
F.D. Stacey, Rep. Prog. Phys. 68 (2005) 431;
G. Parsafar, N. Farzi, B. Najafi, Int. J. Thermophys. 18 (1997) 1197;
V.G. Baonza, M. Cáceres, J. Núñez, Phys. Rev. B 51 (1995) 28;
E.M. Holleran, Thermoch. Acta 59 (1982) 167.
[2] S. Taioli, C. Cazorla, M.J. Gillan, D. Alfè, Phys. Rev. B 75 (2007) 214103.
[3] B. Li, F. Habbal, M. Ortiz, Int. J. Numer. Math. Eng. 83 (2010) 1541.
[4] B. Li, A. Kidane, G. Ravachandra, M. Ortiz, Int. J. Impact Eng. 42 (2012) 25.
[5] A. Strachan, T. Cagin, O. Gülseren, S. Mukherjee, R.E. Cohen, W.A. Goddard III, Model. Simul. Mater. Sci. Eng. 12 (2004) S445.
[6] J.A. Moriarty, J.F. Belak, R.E. Rudd, P. Söderlind, F.H. Streitz, L.H. Yang, J. Phys.: Condens. Matter 14 (2002) 2825.
[7] P. Hohenberg, W. Kohn, Phys. Rev. B 136 (1964) B864.
[8] W. Kohn, L.J. Sham, Phys. Rev. B 140 (1965) 1133.
[9] R. Jones, O. Gunnarsson, Rev. Mod. Phys. 61 (1989) 689.
[10] J.P. Perdew, et al., Phys. Rev. B 46 (1992) 6671.
[11] A.D. Becke, Phys. Rev. A 38 (1988) 3098.
[12] D.C. Langreth, M.J. Mehl, Phys. Rev. B 28 (1983) 1809.
[13] S. Taioli, C. Cazorla, M.J. Gillan, D. Alfè, J. Phys.: Conf. Ser. 121 (2008) 012010.
[14] C.J. Wu, P. Söderlind, J.N. Glosli, J.E. Klepeis, Nat. Mater. 8 (2009) 223.
[15] L. Burakovsky, et al., Phys. Rev. Lett. 104 (2010) 255702.
[16] J.B. Haskins, J.A. Moriarty, R.Q. Hood, Phys. Rev. B 86 (2012) 224104.
[17] B. Boates, S.A. Bonev, Phys. Rev. Lett. 102 (2009) 015701.
[18] I. Iosilevski, V. Gryaznov, in: Proceedings of International Conference on HIF-

2002, ITEP Publishing, Moscow, 2010.
[19] V. Ternovoit, et al., High Temp.-High Press. 37 (2008) 267.
[20] C.W. Greeff, J.D. Johnson, LA-13681-MS, 2000.
[21] I.V. Lomonosov, et al., AIP Conf. Proc. 620 (2002) 111.
[22] P.R. Levashov, et al., AIP Conf. Proc. 505 (2000) 89.
[23] D.A. Young, B.J. Alder, Phys. Rev. A 3 (1971) 364.
[24] G.R. Gathers, Rep. Prog. Phys. 49 (1986) 341.
[25] A.A. Likalter, Physica A 311 (2002) 137.
[26] V.E. Fortov, I.T. Yacubov, Physics of Nonideal Plasmas, Hemisphere Publishing, New York, 1989.
[27] G. Kresse, J. Hafner, Phys. Rev. B 47 (1993) 558;
G. Kresse, J. Hafner, Phys. Rev. B 49 (1994) 14251;
G. Kresse, J. Furthmüller, Comput. Mater. Sci. 6 (1996) 15;
G. Kresse, J. Furthmüller, Phys. Rev. B 54 (1996) 11169.
[28] P.E. Blöchl, Phys. Rev. B 50 (1994) 17953;
G. Kresse, D. Joubert, Phys. Rev. B 59 (1999) 1758.
[29] J.P. Perdew, K. Burke, M. Ernzerhof, Phys. Rev. Lett. 77 (1996) 3865.
[30] D. Frenkel, B. Smit, Understanding Molecular Simulation, Academic Press, San Diego, 1996.
[31] O. Sugino, R. Car, Phys. Rev. Lett. 74 (1995) 1823.
[32] G.A. de Wijs, G. Kresse, M.J. Gillan, Phys. Rev. B 57 (1998) 8223.
[33] Q.-J. Hong, A. van de Walle, J. Chem. Phys. 139 (2013) 094114.
[34] A. van de Walle, J. Phase Equilib. 33 (2009) 266.
[35] S. Mukherjee, R.E. Cohen, O. Gülseren, J. Phys.: Condens. Matter 15 (2003) 855.
[36] J.W. Edwards, R. Speiser, H.L. Johnston, J. Appl. Phys. 22 (1950) 424.
[37] D. Errandonea, M. Somayazulu, D. Häusermann, H.K. Mao, J. Phys.: Condens. Matter 15 (2003) 7635.
[38] A.B. Belonoshko, et al., Phys. Rev. B 73 (2006) 012201.
[39] D. Alfè, C. Cazorla, M.J. Gillan, J. Chem. Phys. 135 (2011) 024102.
[40] A.B. Belonoshko, T. Lukinov, L. Burakovsky, D.L. Preston, A. Rosengren, Eur. Phys. J. Spec. Top. 216 (2013) 199.
[41] A. van de Walle, G. Ceder, J. Phase Equilib. 23 (2002) 348.
[42] L.-G. Wang, A. van de Walle, Phys. Chem. Chem. Phys. 14 (2012) 1529.
[43] A.T. Dinsdale, CALPHAD: Comput. Coupl. Phase Diagrams Thermochem. 15 (1991) 317.
[44] R. Hultgren, et al., Selected Values of the Thermodynamical Properties of the Elements, American Society for Metals, Metals Park, OH, 1973.
[45] J.M. Brown, J.W. Shaner, Rarefaction velocities in shocked tantalum and the high pressure melting point, in: J.R. Asay, R.A. Graham, G.K. Struab (Eds.), Shock Waves in Condensed Matter, Elsevier, New York, 1984.
[46] J.W. Shaner, R.G. Gathers, C. Minichino, High Temp.-High Press. 9 (1977) 331.
[47] L.-G. Wang, A. van de Walle, D. Alfè, Phys. Rev. B 44 (2011) 092102.
[48] Q.-J. Hong, A. van de Walle, J. Chem. Phys. 137 (2012) 094114.
[49] A. van de Walle, Science 346 (2014) 704.
[50] Q.-J. Hong, S.V. Ushakov, A. Navrotsky, A. van de Walle, Acta Mater. 84 (2015) 275.
[51] Q.-J. Hong, A. van de Walle, Phys. Rev. B 92 (2015) 020104.
[52] J. Wiebke, P. Schwerdtfeger, G.E. Moyano, E. Pahl, Chem. Phys. Lett. 514 (2011) 164.
[53] B. Efron, Biometrika 68 (1981) 589.
[54] D.Y. Peng, D.B. Robinson, Ind. Eng. Chem., Fundam. 15 (1976) 59.
[55] J. Bohdansky, H.E.J. Schins, J. Phys. Chem. 71 (1967) 215.
[56] E.A. Mason, T.H. Spurling, The Virial Equation of State, Pergamon Press, Oxford, 1969.
[57] J.O. Hirschfelder, C.F. Curtiss, R.B. Bird, The Molecular Theory of Gases and Liquids, John Wiley & Sons, New York, 1964.
[58] M.W. Chase, J. Phys. Chem. Ref. Data Monogr. 9 (1998) 1-1951.
[59] J. Heyd, G.E. Scuseria, M. Ernzerhof, J. Chem. Phys. 118 (2003) 8207.
[60] N.D. Mermin, Phys. Rev. A 137 (1965) A1441.
[61] M.J. Gillan, J. Phys.: Condens. Matter 1 (1989) 689.
[62] D. Alfè, G.D. Price, M.J. Gillan, Phys. Rev. B 64 (2001) 045123.
[63] A. Samanta, M.E. Tuckerman, T.-Q. Yu, W. E, Science 346 (2014) 729.
[64] L. Gómez, A. Dobry, Ch. Geuting, H.T. Diep, L. Burakovsky, Phys. Rev. Lett. 90 (2003) 095701.
[65] O. Sugino, R. Car, Phys. Rev. Lett. 74 (1995) 1823.
[66] G. de Wijs, G. Kresse, M. Gillan, Phys. Rev. B 57 (1998) 8223.
[67] D. Alfè, M. Gillan, G. Price, Nature (London) 401 (1999) 462.